crystals

MDPI

Article

Time-Dependent Study of Inclusions in Bearing Steel Subjected to Rare Earth Treatment with Secondary Oxidation

Weining Wang, Wenzhi Xia, Yun Zhou *, Aijun Deng, Guangda Bao, Zhiyou Liao * and Haichuan Wang *

School of Metallurgical Engineering, Anhui University of Technology, Maanshan 243032, China; wangweiwang_1985@126.com (W.W.)

* Correspondence: zhouyun@ahut.edu.cn (Y.Z.); lzhy@ahut.edu.cn (Z.L.); which@ahut.edu.cn (H.W.)

Abstract: Due to the strong reducibility and chemical activity of rare earths, the diffusion behavior and secondary oxidation of rare earths in the steel liquid will also have a significant impact on the modified products when rare earths are added to bearing steel, resulting in poor control of distribution behavior. Therefore, this paper studies the influence of time factors on the evolution of rare earth inclusions. The inclusion evolution behavior at different times when the bearing steel was treated with rare earths and subjected to secondary oxidation was simulated at 1873 K (1600 °C). At a cerium content of 0.012% in steel and a secondary oxidation of 0.0025%, the cerium content in steel and the total oxygen (T.O.) content in steel were determined at the 30 s, 3 min, 5 min, and 7 min after the addition and the inclusions were characterized by automatic scanning electron microscopy. The results demonstrated the formation of a cerium-enriched zone after the addition of the cerium alloy to the steel. As time progressed, a considerable number of inclusions were generated in the cerium-enriched zone, which subsequently disappeared. The trend in the composition of the inclusions can be described as $Al_2O_3 \rightarrow Ce_2O_2S + CeS \rightarrow Ce_2O_2S$. The final composition of the inclusions matches the thermodynamic phase diagram. Following the addition of the transient oxidant Fe_2O_3 to the molten steel, an oxygen-enriched zone was formed. As time progressed, a considerable number of inclusions were generated in the oxygen-enriched zone and subsequently disappeared. The trend of inclusions composition was as follows: $Ce_2O_3 + CeAlO_3 + Al_2O_3 \rightarrow Ce_2O_3 + CeAlO_3 \rightarrow Ce_2O_2S + CeAlO_3$. The final inclusion composition coincides with the thermodynamic phase diagram.

Keywords: rare earth inclusions; secondary oxidation; transient oxidation; bearing steel; time

check for updates

Citation: Wang, W.; Xia, W.; Zhou, Y.; Deng, A.; Bao, G.; Liao, Z.; Wang, H. Time-Dependent Study of Inclusions in Bearing Steel Subjected to Rare Earth Treatment with Secondary Oxidation. *Crystals* **2024**, *14*, 697. https://doi.org/10.3390/cryst14080697

Academic Editor: Benilde F. O. Costa

Received: 8 July 2024
Revised: 25 July 2024
Accepted: 27 July 2024
Published: 30 July 2024

Copyright: © 2024 by the authors. Licensee MDPI, Basel, Switzerland. This article is an open access article distributed under the terms and conditions of the Creative Commons Attribution (CC BY) license (https://creativecommons.org/licenses/by/4.0/).

1. Introduction

The utilization of rare earths to modify inclusions in steel [1–20] was occasionally associated with generating heterogeneous [21,22] and unstable properties within the steel. In addition to the number of rare earth elements introduced, the diffusion behavior and secondary oxidation of rare earth [23] in the molten steel will also have a significant impact on the composition of the resulting modification products. When rare earth metals are added to the molten steel, they react with the oxygen and inclusions present in the molten steel. This reaction occurs too rapidly in the molten steel to allow for homogenization, thereby leading to the retention of the rare earth reaction products. During the actual production process, the initial pouring of molten steel from the furnace inevitably leads to secondary oxidation. It results in the formation of a significant number of oxidized inclusions, which in turn causes notable changes in their composition, quantity, and size, thereby affecting the uniformity of their distribution.

Zhang Yuexin et al. [24] examined the composition and morphology of inclusions in solid unoriented electrical steel before and after heating and analyzed the transformation of $LaAlO_3$ inclusions during heating. Ren Q et al. [25] investigated the transient effect of Ce on inclusions in aluminum sedum unoriented electrical steel and derived different modifications of rare earth inclusions corresponding to different Ce contents at different

moments. Ren Qiang et al. [26] conducted laboratory experiments at 1873 K (1600 °C) to investigate the effect of Ce on inclusions in ultra-low carbon aluminum sedimented steel. The concentration of Ce in the steel ranged from 0 to 0.028%. The total oxygen (T.O), total nitrogen (T.N), total sulfur (T.S), total cerium (T.Ce), and dissolved aluminum ([Al]) contents were determined in steel samples at 1, 5, 10, and 30 min after the addition of Ce and the inclusions were characterized using an automated scanning electron microscope. The result shows that the composition of the inclusions exhibited a gradual transition from $Al_2O_3 \rightarrow CeAlO_3 \rightarrow Ce_2O_2S \rightarrow Ce_2O_2S + CeS$ as the Ce content increased. In a study by Li Bin et al. [27], the evolution of inclusions in high alumina steels was investigated following the addition of La. A series of laboratory experiments and thermodynamic calculations were conducted to consider the reaction time and the amount of La added. For La additions of less than 0.0041 wt%, the evolution pathway of inclusions in high alumina steel was $Al_2O_3 \rightarrow LaAl_{11}O_{18} \rightarrow LaAlO_3$, with increasing reaction time. For high La additions, the evolution pathway of Al_2O_3 inclusions was as follows: $Al_2O_3 \rightarrow LaAl_{11}O_{18} \rightarrow LaAlO_3 \rightarrow La_2O_2S \rightarrow La_2S_3$. Wang Yoguang et al. [28] conducted two industrial furnace tests to investigate the effect of secondary oxidation on the characteristics of rare earth aluminum sedum steel inclusions during casting. The tests employed RH, intermediate ladle, immersion spout, and slab sampling for stable casting and secondary oxidation. Consequently, the number of inclusions increased significantly and the near-spherical Ce_2O_2S inclusions were transformed into clustered $CeAlO_3$, which increased the average size of inclusions from 3.92 μm to 9.21 μm. Thermodynamic calculations indicated that with varying Ce additions, an increase in total oxygen content (T.O.) facilitated the transformation of Ce_2O_2S to $CeAlO_3$. However, there is a lack of studies on the uniformity of inclusion distribution. While most published research focuses on thermodynamic or experimental analyses, there are few studies that combine experimental data with thermodynamic analyses, especially those examining inclusions at various time points in bearing steel melts subjected to rare earth treatments and secondary oxidation processes. This study utilized thermal state experiments to simulate the modification of inclusions in bearing steel at various time points after rare earth treatment and secondary oxidation. Combined with thermodynamic calculations, the study analyzed the evolution mechanism and control conditions of inclusion modification over time. This analysis aims to offer theoretical guidance for enhancing the uniformity of inclusion distribution and the stability of steel properties.

2. Materials and Methods

2.1. Thermodynamic Simulation

The thermodynamic simulation was aimed at studying the evolution mechanism of inclusions in bearing steel after adding rare earth elements and the evolution mechanism of inclusions during the secondary oxidation process of bearing steel treated with rare earth elements. The equilibrium module of FactSage 8.2 software (FactSage is the result of over 20 years of collaborative efforts between Thermfact/CRCT (Montreal, QC, Canada) and GTT-Technologies (Aachen, Germany)) was utilized alongside the FactPS, Ftoxide, and FTsteel databases. A thermodynamic model was established using pure solid and solution phases to calculate the equilibrium between the steel liquid and inclusions at 1873 K (1600 °C). Through rigorous data comparisons for Ce_2O_2S, information from the "Thermochemical data of elements and compounds" database was selected, which includes heat capacity, entropy, enthalpy change data, and corresponding calculated Gibbs free energy changes.

2.2. Vacuum Induction Furnace Experiment

The following two simulation experiments were carried out to study the formation mechanism of inclusions in rare earth-treated bearing steel.

(A) Experiments with instantaneous addition of 0.01% rare earth Ce content at an initial oxygen content of 0.001%.

(B) Based on the first experiment, Fe_2O_3 powder was used as an external O source to provide a secondary oxidation environment and increase the melt oxygen content to induce secondary oxidation. The specific addition amount was calculated according to the reaction equation (Fe_2O_3) = 2[Fe] + 3[O] and the secondary oxygen content was 0.0025%.

Experiment A: The melting process was as follows. (1) The bearing steel raw material was placed into the MgO crucible after removing the surface oil and iron oxide skin with a grinder. The rare earth ingot was polished with sandpaper, then weighed and treated with vacuum packaging to prevent oxidation. The rare earth Ce and Al grains were put into the container of the vacuum induction furnace and then prepared for melting. (2) Turn on the power supply and vacuum valve and evacuate the vacuum to 10 Pa; then fill the chamber with argon to protect the melt from oxidation. (3) Turn on the water and then the power and start to enter the melting period to ensure that the charge is fully melted. (4) After the melting period, the temperature reached 1873 K, the power supply was maintained at a stable level, and the melt was held for 10 min to ensure that a stable melt temperature was achieved. (5) After the end of the holding period, aluminum grains were added and held for 5 min, the sampling rod was lowered, and the first sample was taken using a glass tube sampler. The weighed rare earth was then added to the melt. At 30 s as well as 3, 5, and 7 min, the sampling rod was lowered to the same height and the fourth process sample was taken using a glass tube sampler. For each sampling process, the sampling tube was kept in the same orientation and depth from the bottom of the steel to ensure the same sampling position. In addition, to preserve the original composition and morphology of the inclusions in the steel and to prevent the steel from producing new precipitates during cooling and solidification, the molten steel samples were quenched in cold water immediately after removal from the molten steel.

The melting steps in experiment B were as follows: the pre-process was the same as (1), (2), (3), and (4) in experiment A. Then (5) after the end of holding, add aluminum particles, hold for 5 min, and drop the sampling rod using a glass tube sampler to take an experimental sample. Then, the weighed rare earth was added to the melt. After waiting for 10 min, the sampling rod was lowered to the same height and the first experimental sample was taken with a glass tube sampler. (6) The weighed Fe_2O_3 powder was added to the melt. At 30 s as well as 3, 5, and 7 min, the sampling rod was lowered to the same height and the fourth process sample was taken with a glass tube sampler. For each sampling, the sampling tube was held in the same direction and depth from the bottom of the steel to ensure the same sampling position. In addition, to preserve the original composition and morphology of the inclusions in the steel and to prevent the steel from producing new precipitates during cooling and solidification, the molten steel samples were quenched in cold water immediately after removal from the molten steel. The experimental setup is shown in Figure 1.

High carbon chromium-bearing steel (GCr15) from a steel mill with the composition shown in Table 1 was used for the experiments. Pure aluminum was used as the deoxidizer during the experiment (A198%, Si0.6%, and Fe0.7%). The rare earth raw material was high-purity rare earth Ce with a purity of 99.98%, a melting point of 798 °C, and a boiling point of 3426 °C.

Table 1. Chemical composition of bearing steel used in the experiment (mass fraction, %).

Heat Number	C	Si	Mn	P	S	O	Cr	Ni	Al	Ce
a	0.995	0.23	0.344	0.005	0.003	0.0010	1.418	0.018	0.014	0.012
b	0.991	0.25	0.331	0.003	0.003	0.0025	1.431	0.018	0.014	0.012

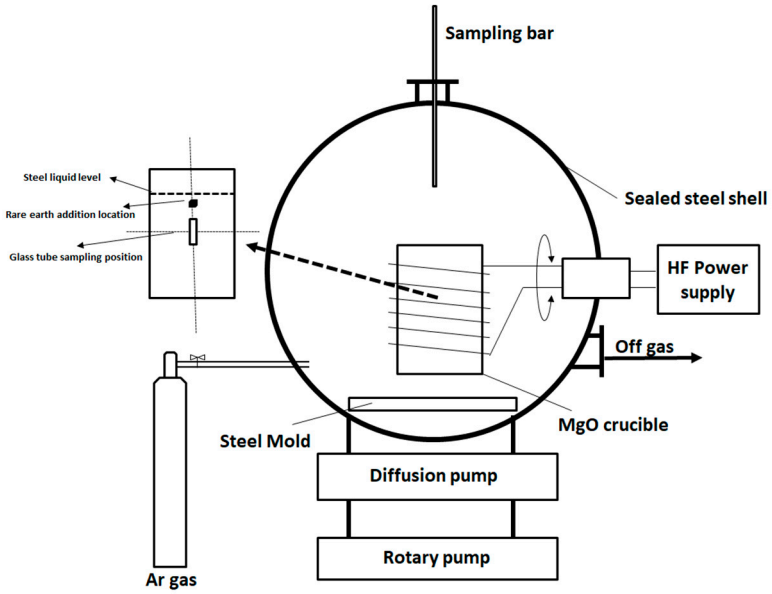

Figure 1. Schematic of the experimental setup.

2.3. Testing Methods

The oxygen content was determined using an EMGA-820 oxygen and nitrogen analyzer, whereas the rare earth content in the bearing steel was assessed using a 5110 ICP-OES mass spectrometer. For the analysis and statistical assessment of inclusions larger than 1 μm in steel, the OPTON inclusions automatic analysis scanner was employed. The scanning field of view covered an area of 4,000,000 μm^2 and analysis was carried out by the GB/T 30834-2014 [29] standard, utilizing a magnification of 1000 times. The evolution of the composition, quantity, and size of the inclusions in different samples was investigated using SEM-EDS. This approach allowed observation of the morphology of the inclusions or clusters. Additionally, Image-Pro Plus 6.0 Image analysis and processing software were utilized to analyze the size of the inclusions in the captured images. These comprehensive analytical techniques offer detailed insights into variations in the composition, quantity, and size of inclusions across various samples.

3. Results and Discussion

3.1. Rare Earth Treatment of Bearing Steel

3.1.1. Thermodynamic Simulation of Rare Earth Treatments

Figure 2 illustrates the changes in thermodynamic equilibrium within the molten steel as the rare earth Ce content increases, with an initial oxygen content of 0.001% and a temperature of 1873 K. A specific experimental composition, Fe-0.995C-0.23Si-0.344Mn-1.42Cr-0.018Ni-0.25Cu-0.003S-0.005P-0.0015N-0.014Al-0.0033Ti, was chosen for simulation.

At a temperature of 1873 K, the inclusion curve in the figure shows that in the absence of rare earth additions, the inclusions in the steel were Al_2O_3. As the Ce content increased, the Al_2O_3 inclusion content decreased linearly, concurrently with the formation and gradual increase in rare earth inclusions, $CeAlO_3$ and $CeAl_{11}O_{18}$. With further increases in rare earth Ce content, $CeAl_{11}O_{18}$ reached its maximum at 0.0005% and then gradually decreased. Similarly, $CeAlO_3$ reached its maximum at 0.003% and then decreased. At a rare earth Ce content of 0.0025%, Ce_2O_2S inclusions began to form, transitioning the inclusions from $CeAlO_3$ to a combination of $CeAlO_3$ and Ce_2O_2S. At a Ce content of 0.0115%, CeS inclusions commenced, culminating in the transformation into a combination of Ce_2O_2S and CeS. The evolutionary pathway of inclusions was characterized by a transition from Al_2O_3 to $CeAl_{11}O_{18}$ + $CeAlO_3$, then to $CeAlO_3$ + Ce_2O_2S, followed by Ce_2O_2S, and ultimately to Ce_2O_2S + CeS.

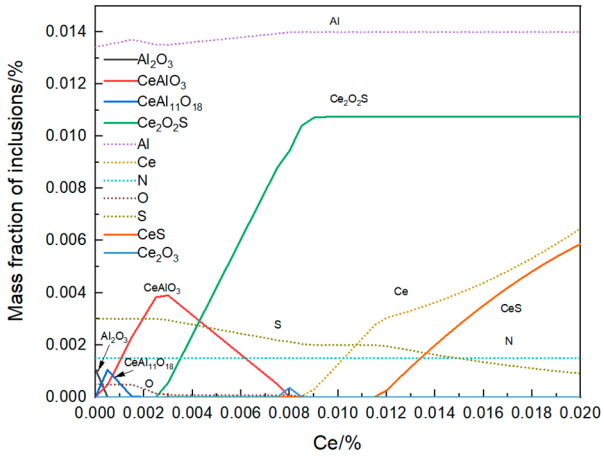

Figure 2. Changes in thermodynamic equilibrium with Ce content.

3.1.2. Rare Earth Vacuum Induction Furnace Trials

When 120 ppm rare earth Ce was added, the sampled inclusions were analyzed and the results are shown in Table 2. At 0 min, the inclusions in the steel were mainly Al_2O_3 inclusions. The shape of the inclusions showed an irregular angular shape, black–grey color, and a large size in Figure 3, of about 1.5 µm. In the 30 s, the morphology and composition of the inclusions in the steel changed significantly and the inclusions in the steel were mainly Ce_2O_2S and CeS. After the addition of rare earth Ce, the inclusions were spherical or spheroidal and the size became fine, about 1 µm. At 3, 5, and 7 min, as shown in Figure 3, many CeS and Ce_2O_2S inclusions were formed and the fine inclusions had a high CeS content. As time increased, these two inclusions were still present in the steel but the number of CeS inclusions decreased and Ce_2O_2S dominated. It could be concluded that when rare earths were added to the steel, the modification law of localized inclusions in the steel increased with time as follows: $Al_2O_3 \rightarrow CeS + Ce_2O_2S \rightarrow Ce_2O_2S + CeS \rightarrow Ce_2O_2S$, as shown in Figure 3.

Table 2. Types of inclusions at different times.

Time	0	30 s	3, 5 min	7 min
Typical inclusions	Al_2O_3	Ce_2O_2S, CeS	Ce_2O_2S, CeS	Ce_2O_2S

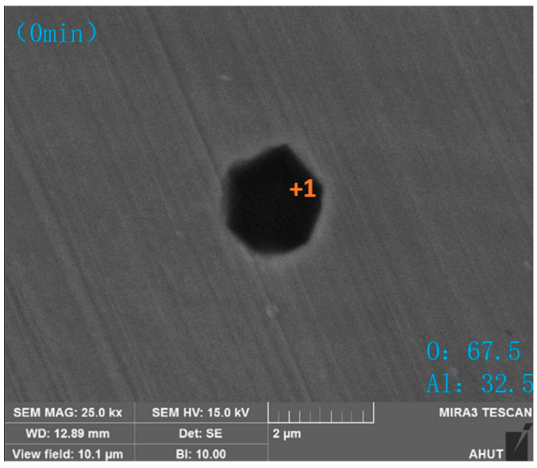

Figure 3. *Cont.*

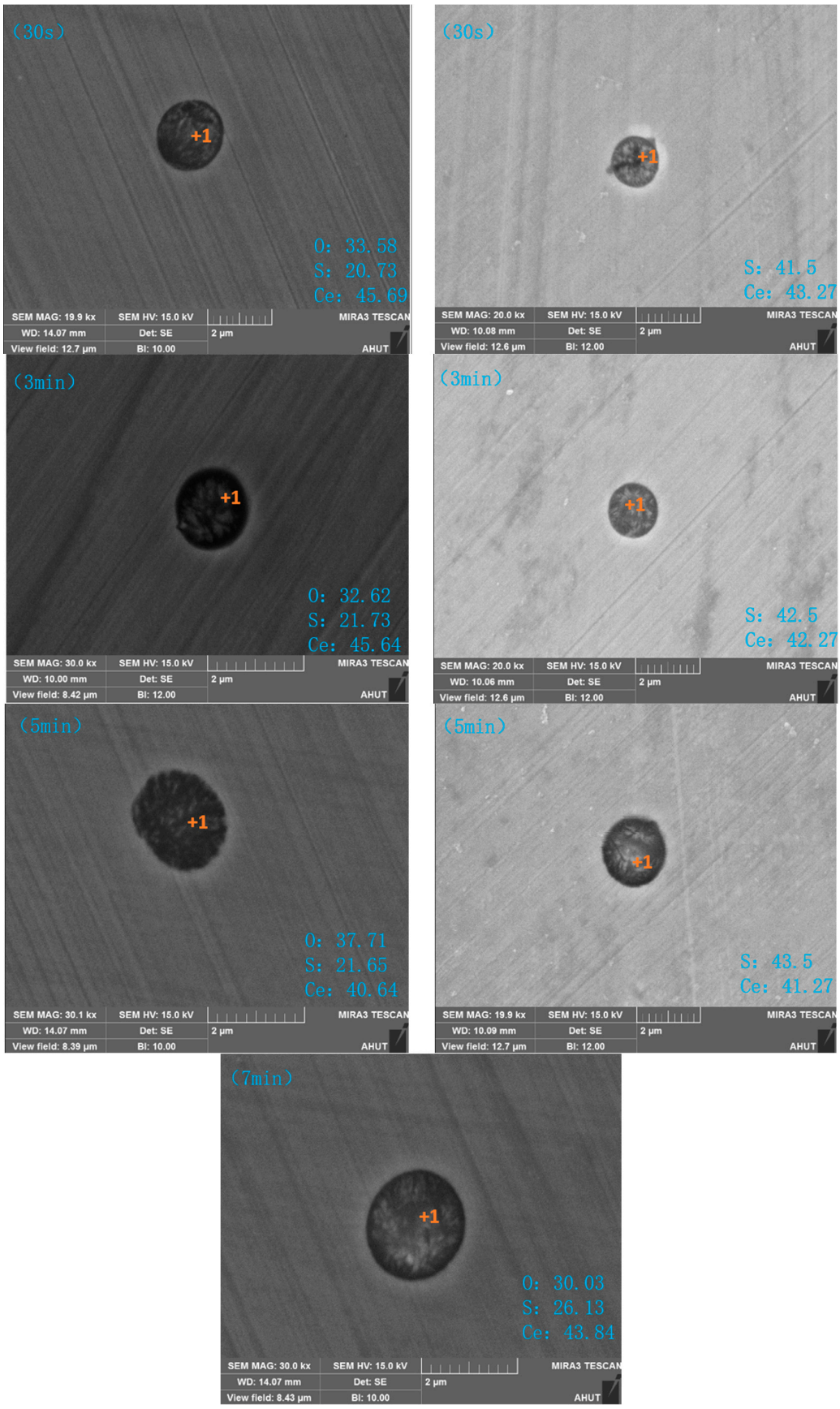

Figure 3. Typical inclusion morphologies at different times after rare earth treatment.

3.1.3. Enrichment Zones Exist in Rare Earth Processing

It is noteworthy that, upon incorporating electron microscopy observations of intermediate samples from vacuum induction furnace experiments, it was discovered that following the addition of Ce, while the final phases remained largely consistent with the corresponding inclusions in the thermodynamic phase diagrams, a significant number of CeS inclusions appeared in the intermediate samples. This divergence resulted in a distinct phenomenon between the inclusion types observed in the process samples from the vacuum induction furnace experiments and those predicted by thermodynamic phase diagrams. Therefore, the limitations of thermodynamic calculations in predicting the type of Ce inclusions in steel can be elucidated by considering the dynamics of dissolution diffusion.

(1) Rare earth Ce alloy dissolution and uniform distribution process

After rare earths were dispersed locally throughout the vessel, the addition of the rare earth-Ce alloy caused a significant increase in the local T.Ce content, indicating the formation of a Ce-enriched zone. Over time, the homogenization of Ce within the steel resulted in a decrease in T.Ce content within the fixed measurement region, as depicted in Figure 4. According to the Ce content curve, the peak at 30 s corresponds to the morphology and elemental distribution typical of inclusions observed in steel samples containing 0.0175% Ce, as illustrated in Figure 2. This corresponds to the emergence of CeS inclusions among the observed inclusions.

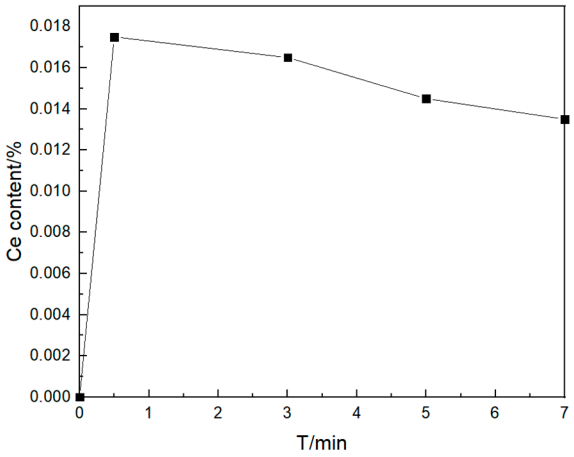

Figure 4. Variation in T.Ce content in steel with time.

(2) Number density, average size, and area density

The number density and average size of inclusions in steel, as depicted in Figure 5, increased after the addition of Ce and then gradually decreased with time. Based on the previous analysis, it was clear that a cerium-enriched zone formed initially after cerium addition. The average size of the inclusions subsequently increased over time.

The area density of inclusions in steel is shown in Figure 6, where the *X*-axis represents the horizontal direction of the photographed area, the *Y*-axis represents the vertical direction of the photographed area, and the *Z*-axis represents the area density of the inclusions. The higher the area density, the greater the number and size of inclusions and the worse the modification effect. After the addition of Ce, the area density of inclusions gradually increased with time.

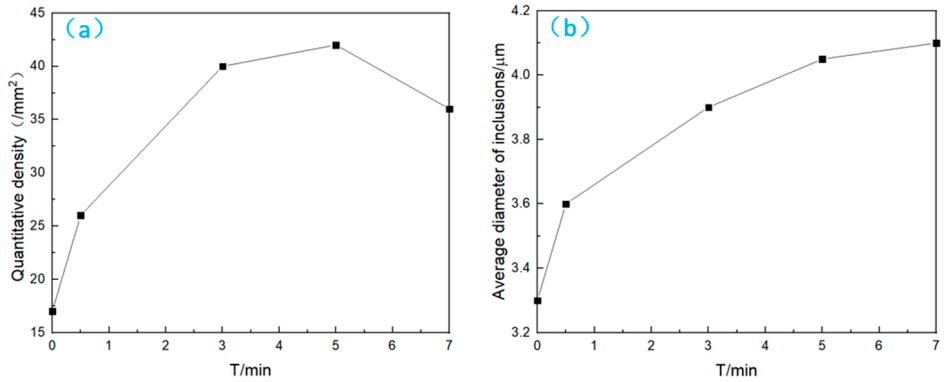

Figure 5. (**a**) Number density and (**b**) average size of inclusions over time.

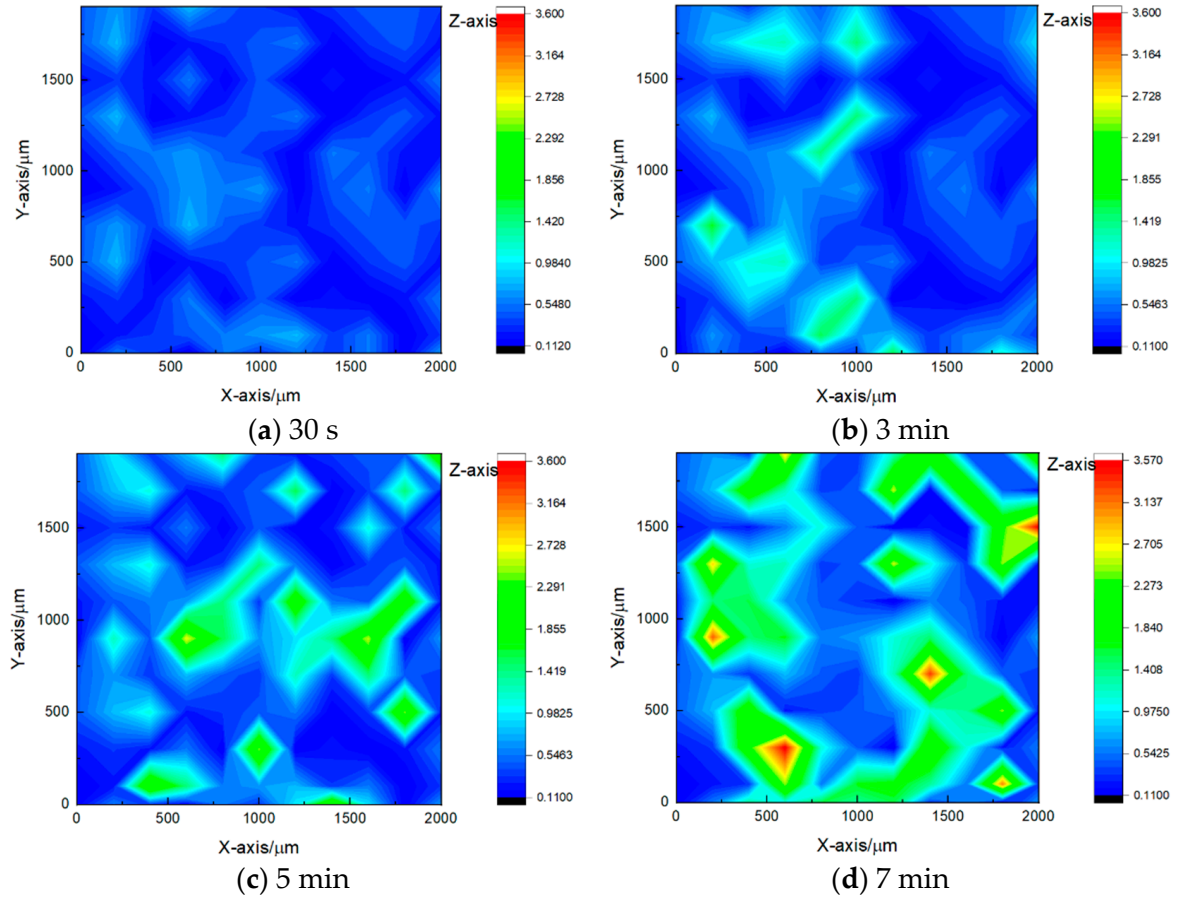

Figure 6. Distribution of area density of inclusions over time.

3.2. Secondary Oxidation

3.2.1. Thermodynamic Simulation of Secondary Oxidation

Figure 7 shows the variation in equilibrium in Fe-0.99C-0.25Si-0.33Mn-1.43Cr-0.004 Al-0.002Ca-0.0005Mg-0.002S-0.012Ce steels with increasing total oxygen (T.O.) at 1873 K (1600 °C). The results indicated that the main inclusions are Ce_2O_2S and CeS at T.O. below 0.0016% and as the T.O. in the steel increases due to secondary oxidation, Ce_2O_2S is gradually converted to $CeAlO_3$.

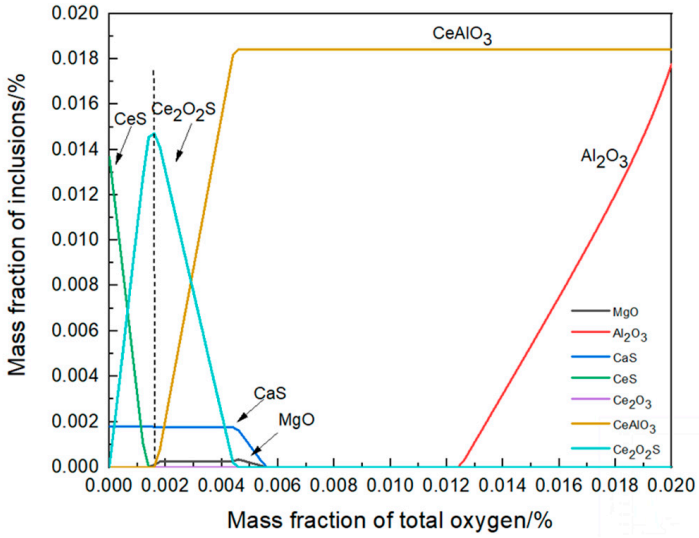

Figure 7. Equilibrium changes with T.O. when the Ce content is 0.0120%.

3.2.2. Secondary Oxidation Vacuum Induction Furnace Experiments

When Fe_2O_3 was added, the sampled inclusions were analyzed and the results are shown in Table 3. At 30, the morphology and composition of the inclusions in the steel changed significantly and the inclusions in the steel were mainly Ce_2O_3, $CeAlO_3$, and Al_2O_3. At 3 min, the inclusions in the steel were mainly Ce_2O_3 and $CeAlO_3$. The shapes of the inclusions in the steel all show obvious spherical or spherical-like shapes and the sizes were small, about 1.5 μm. At 5 and 7 min, the inclusions in the steel were mainly Ce_2O_2S and $CeAlO_3$ but the number of Ce_2O_2S gradually increased and the number of $CeAlO_3$ decreased. It can be concluded that when rare earths were added to steel, the modification law of local inclusions in steel increased with time as follows: $Ce_2O_3 + CeAlO_3 + Al_2O_3 \rightarrow Ce_2O_3 + CeAlO_3 \rightarrow Ce_2O_2S + CeAlO_3$, as shown in Figure 8.

Table 3. Types of inclusions at different times.

Time	30 s	3 min	5, 7 min
Typical inclusions	Ce_2O_3, $CeAlO_3$, Al_2O_3	Ce_2O_3, $CeAlO_3$	Ce_2O_2S, $CeAlO_3$

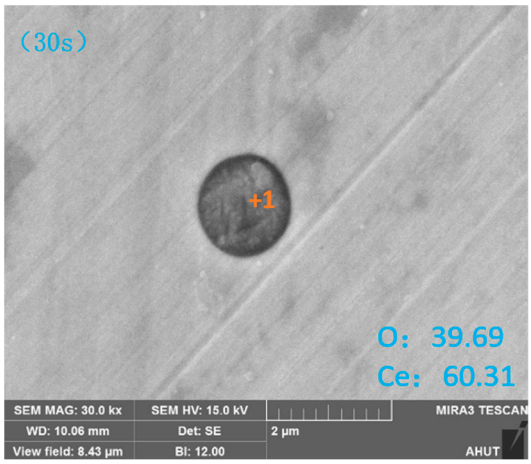

Figure 8. *Cont.*

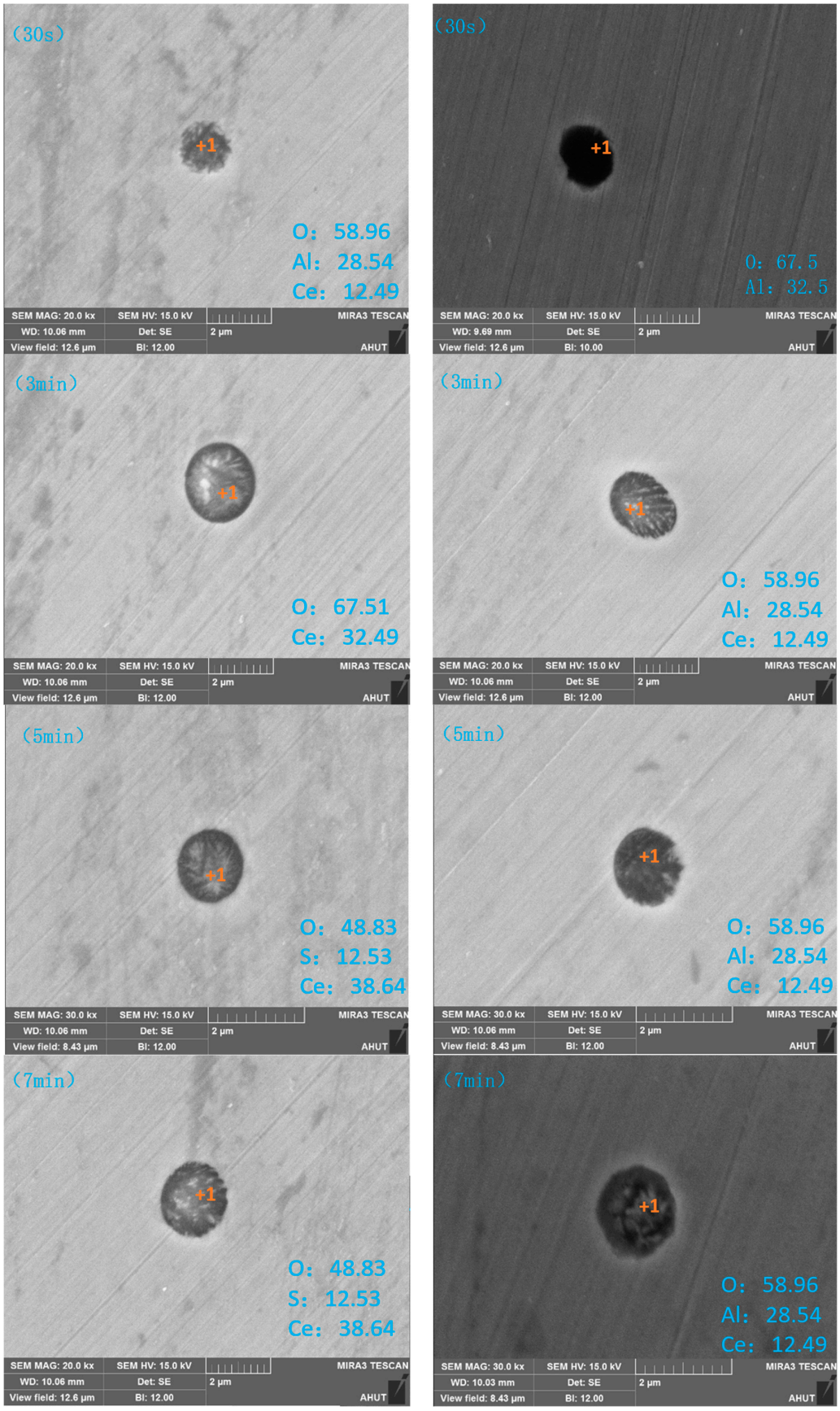

Figure 8. Typical inclusion morphologies at various times after secondary oxidation.

3.2.3. Enrichment Zones Exist during Secondary Oxidation

The secondary oxidation process, similar to the rare earth treatment process for bearing steel, also manifested during the vacuum induction furnace experiments when sampling inclusions. Interestingly, discrepancies arose between the types of inclusions observed and those predicted by thermodynamic phase diagrams. While the final stage and thermodynamic phase diagrams aligned in terms of inclusion types, discrepancies emerged in the intermediate stages. This phenomenon can also be attributed to the kinetic aspects of dissolution diffusion.

(1) Change the curve of oxygen content

Since the Fe_2O_3 powder was dispersed from the local area to the entire vessel after it was added to the steel, the T.O. content in the local area increased sharply when Fe_2O_3 powder was added to the steel, reaching a high value. Then, it gradually decreased as time elapsed. This indicated the presence of an oxygen-enriched region following the addition of Fe_2O_3. With time, the homogenization of O in the steel led to a decrease in the T.O. content in the fixed measurement region, as shown in Figure 9.

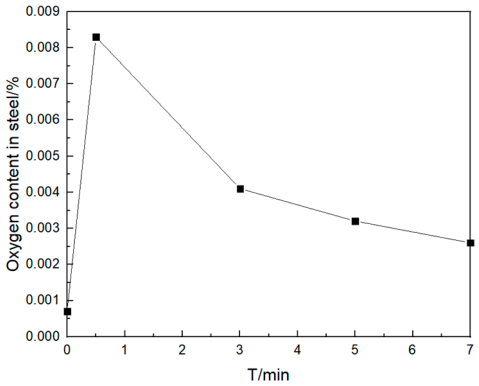

Figure 9. Changes in oxygen content over time.

(2) Number and area density

Initially, the number density of inclusions was extremely low. When Fe_2O_3 was added, the inclusion number density increased significantly due to the newly formed inclusions resulting from secondary oxidation. The number density rose from 1.2 to 36/mm^2. Three minutes after the addition of Fe_2O_3, the number density decreased to 23/mm^2. The decrease in the number density of inclusions was attributed to the diffusion effect within the steel, facilitating the upward removal and outward diffusion of inclusions. Over time, this led to a progressive reduction in the number density of inclusions. In the final sample, the number density of inclusions decreased to 17/mm^2, as depicted in Figure 10.

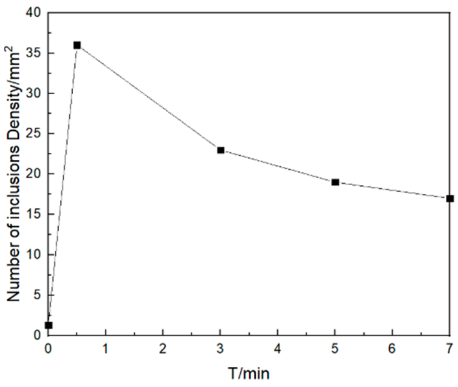

Figure 10. Variation in quantity density of inclusions with time.

The variation in the area density of inclusions in steel is shown in Figure 11, which indicates that the number density and area fraction of inclusions increase in the initial stage (30 s) after the addition of Fe_2O_3 and then decrease with time. From the above analysis, it could be seen that an oxygen-enriched region was formed in the initial stage after the addition of Fe_2O_3.

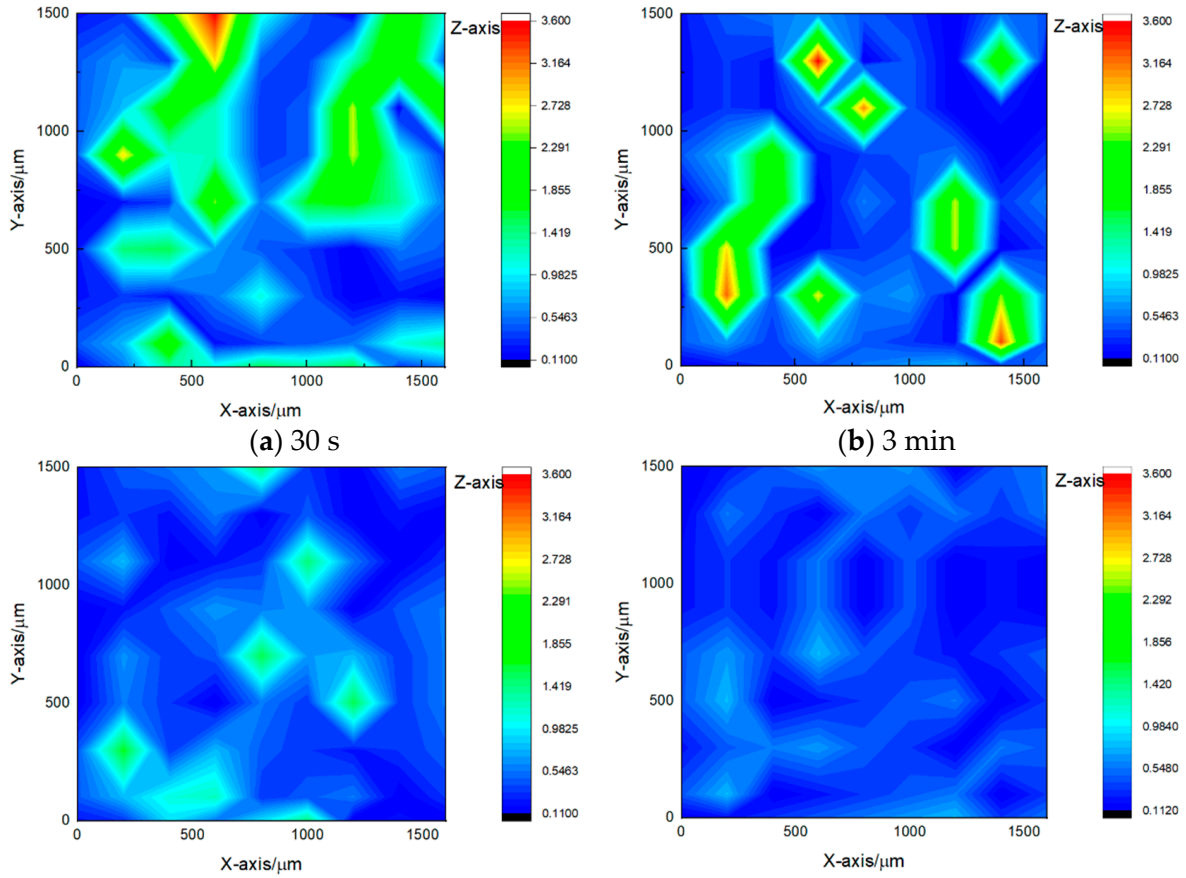

Figure 11. Distribution of the area density of inclusions by time.

(3) Average size and parcel-type inclusions

With time, the average diameter of the inclusions initially increased and then decreased. Specifically, at 30 s after the addition of Fe_2O_3, the average diameter reached 4.6 μm, which was the maximum value. However, as time progressed, the diameter of the inclusions decreased significantly and the average size of the inclusions dropped from the maximum value to 3.52 μm, as depicted in Figure 12.

Following secondary oxidation, there were significant changes in the composition, quantity, and size distribution of the inclusions. A large number of complex inclusions of Ce_2O_2S encapsulated by $CeAlO_3$ were found in the samples, as shown in Figure 13. Together with the replacement of Ce_2O_2S by $CeAlO_3$ inclusions after secondary oxidation shown in Figure 8, these complex inclusions can be considered as an intermediate state in the transition from Ce_2O_2S inclusions to $CeAlO_3$ inclusions, which were formed in large quantities during the secondary oxidation process.

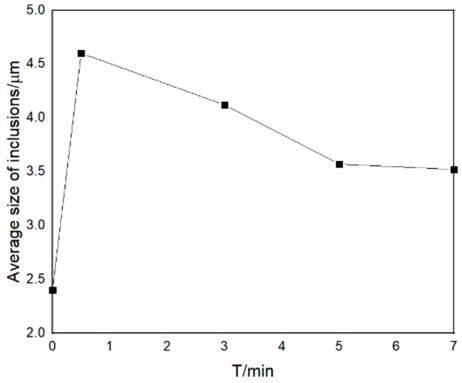

Figure 12. Variation in average inclusion size with time.

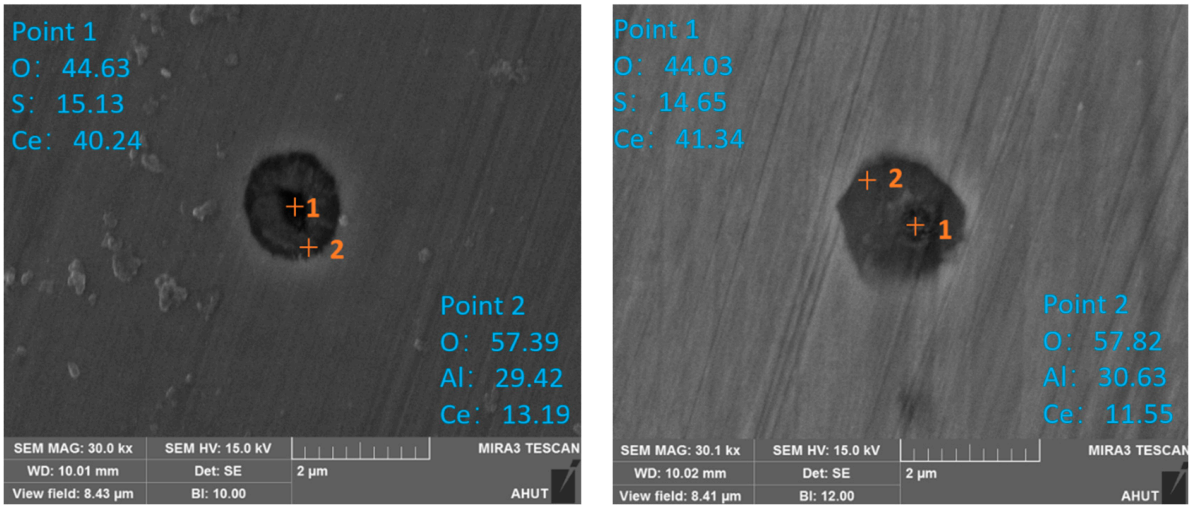

Figure 13. Wrapped inclusions.

4. Conclusions

This study investigated the inclusion evolution behavior at various time points when simulated bearing steel was treated with rare earths and subjected to secondary oxidation. Based on the experimental results and analyses, the main conclusions are as follows:

(1) When the bearing steel is subjected to rare earth Ce treatment, an enriched layer of Ce exists around the rare earth alloy. At a Ce content of 0.012%, the transformation path of inclusions over time is $Al_2O_3 \rightarrow CeS + Ce_2O_2S \rightarrow Ce_2O_2S$. After a certain period, the intermediate sample of inclusions in the vacuum induction furnace is finally in a state consistent with the thermodynamic phase diagram. With time, the number density increases and then decreases, the inclusion size gradually increases, and the area density gradually increases;

(2) In transient secondary oxidation, local steel has an oxygen-rich layer. When the amount of secondary oxidation is 0.0025%, the transformation path of inclusions is $Ce_2O_3 + CeAlO_3 + Al_2O_3 \rightarrow Ce_2O_3 + CeAlO_3 \rightarrow Ce_2O_2S + CeAlO_3$. After a certain period, the intermediate samples of inclusions in the vacuum induction furnace are finally in a consistent state with the thermodynamic phase diagram. With time, the number density and size of the inclusions increase and then decrease and the area density gradually increases;

(3) In the actual production process of bearing steel, when rare earth alloys are added for rare earth treatment, measures should be taken to reduce the influence of rare earth enrichment layers and oxygen enrichment layers.

Author Contributions: Formal analysis, W.W.; Writing—Original Draft, W.W.; Conceptualization, W.W., Y.Z., Z.L. and H.W.; Funding acquisition, Y.Z., Z.L. and H.W.; Project administration, Y.Z., Z.L. and H.W.; Writing—review & editing, Y.Z., Z.L. and H.W.; Data curation, W.X., A.D. and G.B.; Formal analysis, W.X., A.D. and G.B.; Investigation, W.X., A.D. and G.B.; Visualization, W.W., W.X., A.D. and G.B. All authors have read and agreed to the published version of the manuscript.

Funding: This work was supported by the Postdoctoral Fellowship Program of CPSF [grant number GZC20230017]. The APC was funded by Haichuan Wang.

Data Availability Statement: The original contributions presented in the study are included in the article.

Conflicts of Interest: The authors declare that they have no known competing financial interests or personal relationships that may have appeared to influence the work reported in this study.

References

1. Yu, Y.; Feng, X.; Luo, D.; Zhang, Z.; Lai, C. Effect of Rare Earth Ce Addition on Inclusions in Offshore Engineering Steel Containing Arsenic. *Mater. Res. Express* **2023**, *10*, 116512. [CrossRef]
2. Huang, F.; Li, J.; Geng, R.; Wang, C. Effect of Rare Earth on Inclusion Evolution and Corrosion Resistance of HRB400E Steel. *Mater. Corros.* **2023**, *74*, 53–67. [CrossRef]
3. Zhao, B.; Wu, W.; Yang, F.; Zeng, J.; Liang, Z.; He, J. Effect of Cerium Element on Non-Metallic Inclusions Formation During Molten and Solidification Processes of Q355 Microalloy Structural Steel. *Metall. Mater. Trans. B* **2024**, *55*, 1244–1260. [CrossRef]
4. Zhao, Q.; Dong, R.; Lu, Y.; Yang, Y.; Wang, Y.; Yang, X. Effect of Trace Rare-Earth Element Ce on the Microstructure and Properties of Cold-Rolled Medium Manganese Steel. *Metals* **2023**, *13*, 116. [CrossRef]
5. Ye, K.; Cai, X.; Sun, B.; Zhou, L.; Ma, S.; Yue, Y.; Xu, F.; Zheng, D.; Fu, X. Effect of Rare Earth Ce on the Microstructure and Mechanical Properties of Cast Al–7Si Alloys. *J. Sci. Adv. Mater. Devices* **2023**, *8*, 100634. [CrossRef]
6. Bai, G.J.; Yang, J.C.; Liang, W.J. Effect of Lanthanum–Cerium Mixed Rare Earth on Inclusions in U76CrRe Eavy Rail Steel. *Can. Metall. Q.* **2023**, *62*, 720–733. [CrossRef]
7. Bai, G.; Yang, J.; Liang, W. Evaluation and Analysis of the Influence of Rare-Earth Ce on Inclusions in Heavy Rail Steel. *Metals* **2023**, *13*, 614. [CrossRef]
8. Jiang, X.; Li, G.; Tang, H.; Liu, J.; Cai, S.; Zhang, J. Modification of Inclusions by Rare Earth Elements in a High-Strength Oil Casing Steel for Improved Sulfur Resistance. *Materials* **2023**, *16*, 675. [CrossRef] [PubMed]
9. Su, C.; Feng, G.; Zhi, J.; Zhao, B.; Wu, W. The Effect of Rare Earth Cerium on Microstructure and Properties of Low Alloy Wear-Resistant Steel. *Metals* **2022**, *12*, 1358. [CrossRef]
10. Bai, Y.; Zheng, S.; Liu, N.; Liu, Y.; Wang, X.; Qiu, L.; Gong, A. The Role of Rare Earths on Steel and Rare Earth Steel Corrosion Mechanism of Research Progress. *Coatings* **2024**, *14*, 465. [CrossRef]
11. Hao, C.; Wen, J.; Liu, Z.; Yan, J.; Sang, B.; Luan, Y. Effect of Rare-Earth Elements on Fatigue Properties of Spring Steel. *J. Mater. Eng. Perform.* **2024**, 1–10. [CrossRef]
12. Wang, R.; Chen, L.; Zhi, J.; Lian, X.; Guo, L.; Dong, H. Corrosion Behavior of Weathering Steels with Different Contents of Rare Earth Elements La and Ce. *Corrosion* **2022**, *78*, 437–448. [CrossRef]
13. Cao, L.; Zhu, L.; Zhao, R.; Guo, Z.; Qiu, G. Thermodynamics of the Formation of Non-Metallic Inclusions during the Deoxidation of GCr15 Bearing Steel. *Metals* **2023**, *13*, 1680. [CrossRef]
14. Cheng, W.; Song, B.; Yang, Z.; Mao, J. Effect of Rare Earth Ce on Modifying Inclusions in Al-Killed X80 Pipeline Steel. *Trans. Indian Inst. Met.* **2022**, *75*, 2837–2846. [CrossRef]
15. Ren, Q.; Hu, Z.; Cheng, L.; Zhang, L. Effect of Rare Earth Elements on Magnetic Properties of Non-Oriented Electrical Steels. *J. Magn. Magn. Mater.* **2022**, *560*, 169624. [CrossRef]
16. Zhao, Q.; Luo, H.; Pan, Z.; Wang, X.; Cheng, H. Study on Mechanical Properties of Rare Earth Elements Modified High Carbon Chromium Bearing Steel. *Mater. Today Commun.* **2023**, *34*, 105329. [CrossRef]
17. Wang, J.; Peng, J.; Zhang, F.; Li, Y.; Zhang, X.; An, S. Effects of Ce-Modified TiN Inclusions on the Fatigue Properties of Gear Steel 20CrMnTi. *Crystals* **2023**, *13*, 1071. [CrossRef]
18. Zhuo, C.; Liu, R.; Zhao, Z.; Zhang, Y.; Hao, X.; Wu, H.; Sun, Y. Effect of Rare Earth Cerium Content on Manganese Sulfide in U75V Heavy Rail Steel. *Metals* **2022**, *12*, 1012. [CrossRef]
19. Xiaoyu, Z.; Ruifeng, D.; Bo, G.; Jiquan, C.; Zhipeng, M.; Weizhe, Z.; Xiong, Y. Effect of Trace Rare Earth Elements (Ce) on Corrosion Resistance of High Strength Steel Used for Offshore Platform. *Mater. Res. Express* **2023**, *10*, 036514. [CrossRef]
20. Xiao, J.; Yan, L.; Zhang, P.; Li, G.; Li, B.; Zhao, T.; Wang, H.; Chen, L.; Wang, D. Effects of Minor Ce Doping on the Microstructure and Mechanical Performances of an EH47 Grade HSLA Steel for Ship and Ocean Engineering. *Mater. Charact.* **2023**, *201*, 112931. [CrossRef]
21. Cao, Y.; Miao, Y.; Li, D.; Chen, Y.; Fu, P.; Liu, H.; Kang, X.; Liu, H.; Sun, C. On the Mechanism of Steel Homogenization via Rare Earth Addition: Experimental Characterization and Numerical Simulation. *Metall. Mater. Trans. B* **2022**, *53*, 1858–1874. [CrossRef]

22. Duan, R.; Bai, P.; Yang, J.; Zhang, W.; Ding, H. Influence of Rare Earth Modification and Homogenization on the Microstructure and Mechanical Properties of Recycled Can 3004 Aluminum. *J. Wuhan Univ. Technol.-Mater. Sci. Ed.* **2014**, *29*, 264–268. [CrossRef]
23. Liang, W.; Geng, R.; Zhi, J.; Li, J.; Huang, F. Oxide Metallurgy Technology in High Strength Steel: A Review. *Materials* **2022**, *15*, 1350. [CrossRef] [PubMed]
24. Zhang, Y.; Ren, Q.; Kang, X.; Gao, J.; Zhang, L. Transformation of $LaAlO_3$ Inclusions During Heating in a Solid Non-Oriented Electrical Steel. *Metall. Mater. Trans. B* **2022**, *53*, 637–649. [CrossRef]
25. Ren, Q.; Zhang, L.; Hu, Z.; Cheng, L. Transient Influence of Cerium on Inclusions in an Al-Killed Non-Oriented Electrical Steel. *Ironmak. Steelmak.* **2021**, *48*, 191–199. [CrossRef]
26. Ren, Q.; Zhang, L. Effect of Cerium Content on Inclusions in an Ultra-Low-Carbon Aluminum-Killed Steel. *Metall. Mater. Trans. B* **2020**, *51*, 589–600. [CrossRef]
27. Li, B.; Zhu, H.; Zhao, J.; Song, M.; Li, J.; Xue, Z. Effect of Rare-Earth La on Inclusion Evolution in High-Al Steel. *Steel Res. Int.* **2022**, *93*, 2100347. [CrossRef]
28. Wang, Y.; Liu, C. Effect of Reoxidation on Inclusions Characteristic During Casting in Al-Killed Steel Containing Rare Earth. *Steel Res. Int.* **2022**, *93*, 2200263. [CrossRef]
29. *GB/T 30834-2022*; Rating and Classifying of Inclusions in Steel-Scanning Electron Microscrope Method. China Standard Press: Beijing, China, 2022.

Disclaimer/Publisher's Note: The statements, opinions and data contained in all publications are solely those of the individual author(s) and contributor(s) and not of MDPI and/or the editor(s). MDPI and/or the editor(s) disclaim responsibility for any injury to people or property resulting from any ideas, methods, instructions or products referred to in the content.